Effects of metal-based additives on dehydrogenation process of 2NaBH$_4$ + MgH$_2$ system

Yuanyuan Shang[1], Ou Jin[2,3], Julián Atillio Puszkiel[1,4], Fahim Karimi[1], Palmarin Dansirima[5], Chongsutthamani Sittiwet[5], Rapee Utke[5], Siriwat Soontaranon[6], Thi Thu Le[1], Gökhan Gizer[1], Dorothée Vinga Szabó[2,3,7], Stefan Wagner[2], Christian Kübel[2,7,8], Thomas Klassen[1, 3], Martin Dornheim[1], Astrid Pundt[2,3], Claudio Pistidda[1]*

[1] Department of Materials Design, Institute of Hydrogen Technology, Helmholtz-Zentrum hereon GmbH, 21502, Geesthacht, Germany

[2] Institute for Applied Materials, Karlsruhe Institute of Technology, 76131, Karlsruhe, Germany

[3] Institute of Nanotechnology, Karlsruhe Institute of Technology, 76344 Eggenstein-Leopoldshafen, Germany

[4] Helmut Schmidt University, Holstenhofweg 85, 22043, Hamburg, Germany

[5] School of Chemistry, Institute of Science, Suranaree University of Technology, Nakhon Ratchasima 3000, Thailand

[6] Synchrotron Light Research Institute, Nakhon Ratchasima 30000, Thailand

[7] Karlsruhe Nano Micro Facility, Karlsruhe Institute of Technology, 76344 Eggenstein-Leopoldshafen, Germany

[8] Joint Research Laboratory Nanomaterials, Technical University of Darmstadt, Darmstadt 64206, Germany

*Correspondence to: claudio.pistidda@hereon.de

Abstract

In this manuscript, we report a systematic investigation of the effect that selected metal-based additives have on the dehydrogenation properties of the reactive hydride composite (RHC) model system 2NaBH$_4$+MgH$_2$. Compared to the pristine system, the material doped with 3TiCl$_3$.AlCl$_3$ exhibits superior dehydrogenation kinetics, particularly during the second dehydrogenation step, *i.e.* the one related to MgB$_2$ formation. The addition of 3TiCl$_3$.AlCl$_3$ alters the controlling mechanism of the second dehydrogenation step making it change from a two-dimensional interface controlled process to a two-dimensional nucleation and growth controlled process. The microstructural investigation of the dehydrogenated 2NaBH$_4$+MgH$_2$ *via* high-resolution transmission electron microscopy (HRTEM) shows significant differences in the MgB$_2$ morphology formed in the doped and undoped systems. The MgB$_2$ has a needle-like structure in the sample doped with 3TiCl$_3$.AlCl$_3$, which is different from the plate-like MgB$_2$ structure in the undoped sample. Moreover, nanostructured metal-based phases, such as TiB$_2$/AlB$_2$ particles, are

also identified for the sample doped with $3TiCl_3.AlCl_3$. These in-situ formed nanoparticles act as heterogeneous nucleation sites for MgB_2, resulting in the kinetic improvement observed in the presence of this unique additive.

1. Introduction

In recent years, the possibility of replacing non-sustainable fossil fuel energy sources with renewable energy sources has been largely debated. In this scenario, hydrogen is considered as a potential energy vector capable of supporting this epochal transition[1-4]. Hydrogen has the highest energy density per mass, *i.e.*, almost 2.5 times of the energy density per mass of conventional fossil fuels such as methane, propane, and gasoline. As an example, under ambient conditions, the mass-energy density of hydrogen is ~ 120 MJ·kg^{-1}, while the values for methane, gasoline, and diesel are about 55.6, 46.4, and 45.6 MJ·kg^{-1}, respectively[5]. However, hydrogen being the lightest element on the periodic table, its energy density per volume (0.003 kWh·L^{-1})[6] is lower than the volumetric energy densities of methane, propane, and gasoline (4.2, 7.1, and 9.0 kWh·L^{-1}, respectively[7,8]). To overcome the volumetric energy density handicap, hydrogen is commonly compressed to pressures up to 700 bar or liquefied at cryogenic temperatures (*i.e.*, -253 °C), through energy-demanding processes. For instance, the theoretical energy values spent for the isothermal compression of hydrogen up to 350 and 700 bar are 12% and 15% of its lower heating value (LHV), respectively, while 30% of its LHV is necessary for liquefaction[9]. An alternative method is to store hydrogen in metal-based compounds chemically. This approach allows storing hydrogen in a solid-state under low working pressure conditions, achieving at the same time high volumetric energy densities and high safety standards[10-21].

The possibility of reversibly storing hydrogen in metal hydrides was investigated in the early 1960s[22]. At that time, the use of complex metal hydrides such as $NaBH_4$, $LiBH_4$, *etc.* to store hydrogen was limited by the apparent irreversibility of their thermal decomposition products[23]. In fact, despite their appealing gravimetric and volumetric hydrogen capacity, complex metal hydrides are reversible only at extreme temperature and hydrogen pressure conditions. For instance, $LiBH_4$ could be partially rehydrogenated at 600 °C under 350 bar of hydrogen pressure[24]. For this reason, until the end of the 1990s, they mainly were investigated as one-pass storage systems. The one-pass storage method releases hydrogen upon water hydrolysis[23,25] in the presence of transition metal-based catalysts. In 1996 the pioneering work of Bogdanovic and Schwickardi[26] opened the doors to the use of complex metal hydrides as reversible hydrogen storage systems. Since then, many efforts have been made to investigate the properties of this class of hydrides and to optimize their performance by using suitable catalysts and destabilizing agents[27,28].

As the result of this investigation effort, the reactive hydride composites (RHCs) approach was discovered. In this approach, two or more hydride species are combined to obtain a system

with a still high hydrogen storage capacity but lower reaction enthalpy and high reversibility[29-35]. One of the RHCs that has been considered as a model system is $2NaBH_4 + MgH_2$[36-43]. In this system, the dehydrogenation is expected to occur following a two-step reaction[37,40,44-46]:

$$2NaBH_4 + MgH_2 \leftrightarrows 2NaBH_4 + Mg + H_2 \tag{1}$$

$$2NaBH_4 + Mg \leftrightarrows 2NaH + MgB_2 + 4H_2 \tag{2}$$
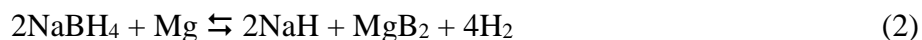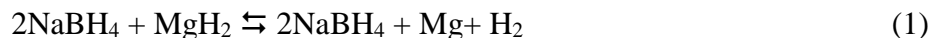
However, depending on the temperature and hydrogen pressure used, reaction intermediates such as the eutectic molten phase of $NaH/NaBH_4$[47], $NaMgH_3$[43], and products such as Na, $NaB_{12}H_{12}$, and B can develop[37,48]. The theoretical dehydrogenation enthalpy for the reaction that from $2NaBH_4 + MgH_2$ lead to $2NaH + MgB_2 + 4H_2$ system is 62 kJ·mol^{-1} H$_2$, 26.2 kJ·mol^{-1} lower than the enthalpy of pure $NaBH_4$[49,50]. Despite the improved thermodynamic stability (lower than that of MgH_2 and $NaBH_4$), the formation of $NaH+MgB_2$ is possible only at elevated temperatures that are still too high for practical application (*i.e.*, 450 °C).

In the attempt to find appropriate catalysts to improve the hydrogen storage properties of RHCs, the use of transition metal (TM)-based additives such as VCl_3, $ZrCl_4$, and Sc_2O_3 proved to be a suitable approach[51-55]. In many cases, by adding small amounts of TM-based additives, the reaction kinetics can be accelerated by a factor of ten[56,57]. For instance, Bösenberg *et al.*[57] found that by adding Sc_2O_3 and $ZrCl_4$ to $2LiBH_4 + MgH_2$, the incubation stage for the dehydrogenation of $LiBH_4$ vanishes, thus the dehydrogenation reaction time is significantly shortened, *e.g.*, from 25 h to 5 h. Karimi *et al.*[58] found that by using the NbF_5 additive, the dehydrogenation temperature of the $Ca(BH_4)_2 + MgH_2$ was decreased from 350 °C to 250 °C. Bonatto Minella *et al.*[55] showed that by adding 5 mol% of TiF_4 into the $Ca(BH_4)_2 + MgH_2$ system, the formation of transition metal boride nanoparticles can be observed, and the onset dehydrogenation temperature decreases from 350 °C to 125 °C. In these works, the added TM-based additives react with the starting materials to form more stable compounds such as ZrB_2 and TiB_2, with an average particle size between 5 and 20 nm. The crystallographic structure and the interface location of those TM-based compounds appear to affect the nucleation and growth of new phases, *e.g.*, MgB_2 in the RHCs. Bösenberg *et al.*[57] proposed that the better nucleation behavior of MgB_2 can be ascribed to the microstructural similarities between the newly generated TM-based phases and the nucleating MgB_2, according to nucleation and growth knowledge accessible from metallurgical areas, *i.e.*, edge-to-edge matching model[59], which was recently further substantiated by Jin *et al.*[60]. For heterogeneous nucleation substrates, the coherent energy of the interface between the parental phase and the new phase is minimized by lowering the lattice mismatch at the interface. For example, Jin *et al.*[60] reported the

elastic strain energy density along <10-10>TiB$_2$/AlB$_2$ $\parallel$ <10-10>MgB$_2$ is more than 6 times smaller than that induced at the interface between Mg and MgB$_2$ along <10-10>Mg $\parallel$ <10-10>MgB$_2$. Therefore, the strain energy between the parental phase (TiB$_2$/AlB$_2$) and the new phase (MgB$_2$) can be minimized, and these phases can act as the active nucleation sites for MgB$_2$ to enhance the kinetics for the second dehydrogenation step. Nevertheless, it is not clear if the proposed TM-based additives' mechanism of work also applies to all the RHC systems.

Taking 2NaBH$_4$ + MgH$_2$ as a model system, the present work aims to investigate further the role of the microstructural properties of the additive/additive-derived phases on the nucleation of MgB$_2$. Volumetric technique, X-ray diffraction (XRD), Fourier-transform infrared spectroscopy (FTIR), equilibrium composition calculation, transmission electron microscopy (TEM), and small-angle X-ray scattering (SAXS) method were used to investigate the material properties, with the results reported in the following.

2. Experimental

Commercially available powders of NaBH$_4$ ($\geq$ 98.0% purity, Sigma-Aldrich), MgH$_2$ (95% purity, Rockwood Lithium GmbH), MgF$_2$ (99.99% purity, Umicore Materials AG), 3TiCl$_3$·AlCl$_3$ ($\sim$ 76-78% TiCl$_3$ purity, Fisher Scientific), VCl$_3$ (99% purity, Alfa Aesar), and Mg(OH)$_2$ (95-100.5% purity, Alfa Aesar) were used as starting materials. The specimens investigated in this work were prepared by milling three grams of 2NaBH$_4$ + MgH$_2$ with and without 5 mol% of additives (*i.e.*, MgF$_2$, 3TiCl$_3$·AlCl$_3$, VCl$_3$, and Mg(OH)$_2$) in a Spex 8000M Mixer Mill for 400 min, as shown in Table 1. Stainless steel vial and balls with a diameter of 10 mm were used to perform the milling, with a ball-to-powder ratio of 20:1. The material handling and milling were performed under a continuously purified Ar atmosphere, with H$_2$O and O$_2$ levels lower than 1 ppm.

Table 1 Prepared 2NaBH$_4$+MgH$_2$ RHCs doped with additives.

No.	Composition	Designation
1	2NaBH$_4$ + MgH$_2$	Na-RHC
2	2NaBH$_4$ + MgH$_2$ + 5mol% MgF$_2$	Na-RHC + 5 mol% MgF$_2$
3	2NaBH$_4$ + MgH$_2$ + 5mol% 3TiCl$_3$·AlCl$_3$	Na-RHC + 5 mol% 3TiCl$_3$·AlCl$_3$
4	2NaBH$_4$ + MgH$_2$ + 5mol% VCl$_3$	Na-RHC + 5 mol% VCl$_3$
5	2NaBH$_4$ + MgH$_2$ + 5mol% Mg(OH)$_2$	Na-RHC + 5 mol% Mg(OH)$_2$

The dehydrogenation experiments were carried out using an in-house made Sievert's apparatus. For each analysis, about 170 mg of material were desorbed under 0.15 bar of hydrogen

pressure, increasing the temperature from room conditions to 450 °C with a heating rate of 3 °C/min, and then keeping the material under isothermal conditions at 450 °C for 5 to 8 hours.

The crystalline phase identification was carried out by *ex-situ* powder XRD method using a Bruker D8 Discover diffractometer using Cu-Kα (λ = 1.54184 Å) radiation operated at 1000 mA and 50 kV. The measured 2θ range is 10° to 90° with steps of 10°, for each step, the exposure time is 400 s. To protect the sample from air and moisture, a polymethyl methacrylate (PMMA) airtight sample holder from Bruker was used during the measurements. The average crystallite size was obtained by the full width at half maximum (FWHM) of the diffraction peaks *via* Scherrer formula[62]:

$$t = \frac{0.9\lambda}{\beta \cos\theta} \tag{3}$$

where t is the crystallite size, 0.9 is the particle shape factor, λ is the X-ray wavelength, β is the FWHM, and θ is the Bragg angle.

Fourier transform infrared spectroscopy (FT-IR) technique was applied to characterize the corresponding phases of the as-milled samples, using an Agilent Technologies Cary 620 FT-IR located inside an Ar-filled glovebox (O_2 and H_2O levels lower than 1ppm). Each spectrum was recorded in the range of 650 cm^{-1} to 4000 cm^{-1} with a resolution of 4 cm^{-1}.

Small-angle X-ray scattering (SAXS) measurements were carried out at Beamline 1.3W: SAXS/WAXS, Synchrotron Light Research Institute (SLRI), Thailand. This beamline offers X-ray energy of 9 keV, with a sample-to-detector distance (SSD) of 4297 mm (calibrated using SEBS block co-polymer standard sample). The accessible q-range was between 0.05 and 1.5 nm^{-1}, and the exposure time was chosen to be 60 s. The beam size at the sample position was 1×1 mm^2 and a Rayonix SX165 CCD detector was implemented. The SAXS pattern of the samples and the backgrounds were recorded. These patterns were normalized by the beam intensity and its X-ray transmission. Then, the 1D SAXS profiles were obtained by radial averaging the resultant background-subtracted pattern. Data pre-processing was done *via* software of SAXSIT version 4.48 (Small Angle X-ray Scattering Image Tool, in-house developed software at SLRI).

Equilibrium composition calculations were carried out with the HSC Chemistry software 9.7.2[63]. Pure materials were taken into account for the calculations. The conditions for the calculations were as follows: dehydrogenation from room temperature (RT) to 500 °C under 1 bar of H_2 pressure. The most favorable reactions were identified by combining Gibbs minimization equilibrium with selected solid and gas species. The obtained results represent ideal phase equilibrium compositions useful to predict the possible reaction. The compound $NaMgH_3$ was

added to the database. The enthalpy, entropy, and heat capacity of the $NaMgH_3$ were obtained from ref. [64-66]. All the calculations can be seen in the Supporting information (Fig. S1-10 and Table S1-10).

For the TEM investigations, the sample powder was dispersed in toluene and ultra-sonicated for 1 min at room temperature and subsequently dropped onto Lacey carbon-coated TEM copper grids. To avoid oxidation of the materials, these operations were carried out under argon atmosphere in the glovebox. The prepared sample was then introduced into the TEM column using a vacuum transfer holder 648 (Gatan Inc., USA). TEM experiments were performed on a Themis-Z 60-300 (Thermo Fisher Scientific Inc., USA) equipped with a monochromator and double aberration correctors (probe and image Cs correctors), operated at 300 kV. Scanning TEM (STEM) images and Energy-dispersive X-ray spectroscopy (EDX) elemental mapping were acquired *via* a high-angle annular dark-field (HAADF) detector with a convergence angle of 21.5 mrad and a camera length of 93 mm. Selected area electron diffraction (SAED) patterns and high-resolution TEM (HRTEM) images were recorded using a OneView camera (Gatan Inc., USA).

Kinetic modeling was done by using the Sharp and Jones method[67,68], in which the experimental data can be expressed as follows:

$$F(\alpha) = A\left(\frac{t}{t_{0.5}}\right) \tag{3}$$

where α is the reaction fraction, t is the reaction time, $t_{0.5}$ is the time at $\alpha = 0.5$, and A is the rate constant. $F(\alpha)$ was considered as the hydrogen storage capacity over the maximum capacity for the second dehydrogenation process of each sample. The portion of the dehydrogenation curve used here is $0.1 - 0.7$ (for pure Na-RHC) and $0.1 - 0.8$ (for Na-RHC + 5 mol% $3TiCl_3 \cdot AlCl_3$) of the overall hydrogen storage capacity for the second step. Firstly, the kinetic curves of the second step for each sample were normalized from 0 to 1, as shown in Fig. S12. Subsequently, different fitting models were used to fit the second dehydrogenation step, as shown in Table S11. The criterion for deciding whether a model is feasible is as follows: the slope of the fitted curve should be close to 1, the intercept should be close to 0, and the fitting coefficient of determination (R^2) should be close to 1.

3. Results and discussion

3.1 Structural characterization of the as-milled materials

The diffraction patterns acquired for the as-milled materials are reported in Fig. 1(a). The diffraction peaks that dominate the patterns of $2NaBH_4 + MgH_2$ (Na-RHC), Na-RHC + 5 mol%

3TiCl$_3$·AlCl$_3$, and Na-RHC + 5 mol% VCl$_3$ are those of NaBH$_4$ and MgH$_2$ and in the case of Na-RHC + 5 mol% MgF$_2$ and Na-RHC + 5 mol% Mg(OH)$_2$, the diffraction peaks of Mg are also detectable. The presence of the Mg peaks is expected as it is the main impurity of the purchased MgH$_2$ (purity is 95%). Interestingly, for all the investigated materials, no diffraction signals related to the additives' presence or the products of their interaction with NaBH$_4$ and MgH$_2$ are visible. This can be attributed to the small amount of these compounds or because such compounds are nanostructured after ball milling. Investigations on the possible chemical alteration of the bending and stretching modes of the B-H bonds due to the presence of halogen and oxidize-containing additives were performed. Thus, the as-milled samples were characterized via FT-IR. The obtained FTIR spectra are presented in Fig. 1(b). The features of the [BH4]$^-$ group can be observed in all the spectra, *e.g.*, the B-H bending vibration (~ 1110 cm^{-1}) and the B-H stretching vibrations (2000-2520 cm^{-1}), which is in good agreement with the spectral data from the literature[69,70]. These results show that the B-H bonds in the [BH$_4$]$^-$ groups are unaltered by the addition of the additives and that no H$^-$ to Cl$^-$ or H$^-$ to F$^-$ substitution took place. For what it concerns, the sample containing Mg(OH)$_2$ - although we do not possess direct proof - likely reacted with NaBH$_4$ to form NaOH, B, and H$_2$.
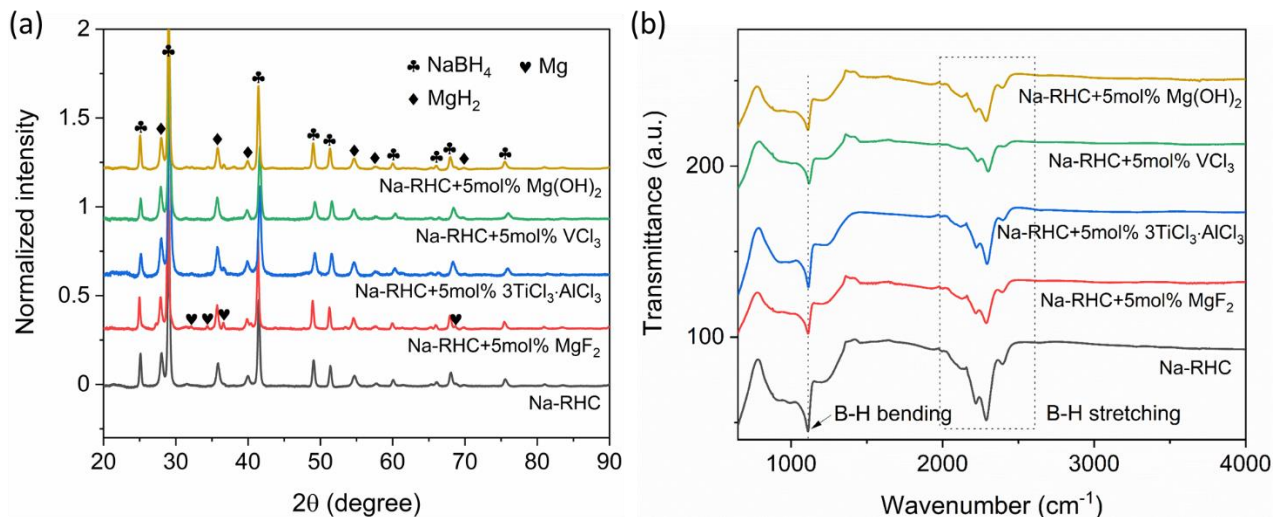
Fig. 1. (a) XRD and (b) FTIR results of as milled Na-RHC + 5 mol% MgF$_2$, 3TiCl$_3$·AlCl$_3$, VCl$_3$, and Mg(OH)$_2$ samples.

3.2 Dehydrogenation investigations

The hydrogen desorption curves of all the Na-RHC samples are shown in Fig. 2(a). As shown in Eqs. (1) and (2), the dehydrogenation process of the Na-RHC consists of two steps. The first

step refers to the dehydrogenation of MgH_2, and the second step corresponds to the dehydrogenation of $NaBH_4$ and the formation of the solid phases NaH and MgB_2. The pure Na-RHC can release 7.5 wt.% of H_2 in 8 h. The sample doped with MgF_2 shows the largest hydrogen release of 8.7 wt.%, while the total hydrogen storage capacity of the material containing $3TiCl_3 \cdot AlCl_3$ is 8.0 wt.%. The sample doped with $Mg(OH)_2$ appears to possess the same hydrogen capacity as the pure Na-RHC, *i.e.*, 7.5 wt.%. The sample doped with VCl_3 has a hydrogen capacity of about 6.7 wt.%. As shown in Fig. 2(a), all additives shortened the incubation time for the first step of dehydrogenation (about 2.1 wt.% of hydrogen is released). Based on the data reported in Fig. 2(a), the magnitude of this effect appears in the following order: $3TiCl_3 \cdot AlCl_3 > VCl_3 > MgF_2 > Mg(OH)_2$. Also, when it comes to the second step, the sample doped with $3TiCl_3 \cdot AlCl_3$ shows the fastest kinetics. Fig. 2(b) shows the XRD patterns acquired for all the samples after dehydrogenation. All the patterns show the characteristic peaks of Na/NaH and MgB_2. The peaks of NaCl or NaF can also be detected in the samples doped with halogen-containing additives. This finding supports our first claim that the halogen-containing phases are nanostructured after milling. Note that for the pristine and $Mg(OH)_2$ doped samples, the diffraction peaks of $NaBH_4$ are still visible, suggesting that the dehydrogenation reaction is not complete, which is in good agreement with the kinetic performances shown in Fig. 2(a). Moreover, based on these data we can safely state that the achievement of capacities higher than expected (*i.e.*, the samples doped with 5 mol% of MgF2 and $3TiCl_3 \cdot AlCl_3$ in Fig. 2(b)) results from the fact that under the applied hydrogen pressure and temperature conditions NaH partially decomposed to Na).

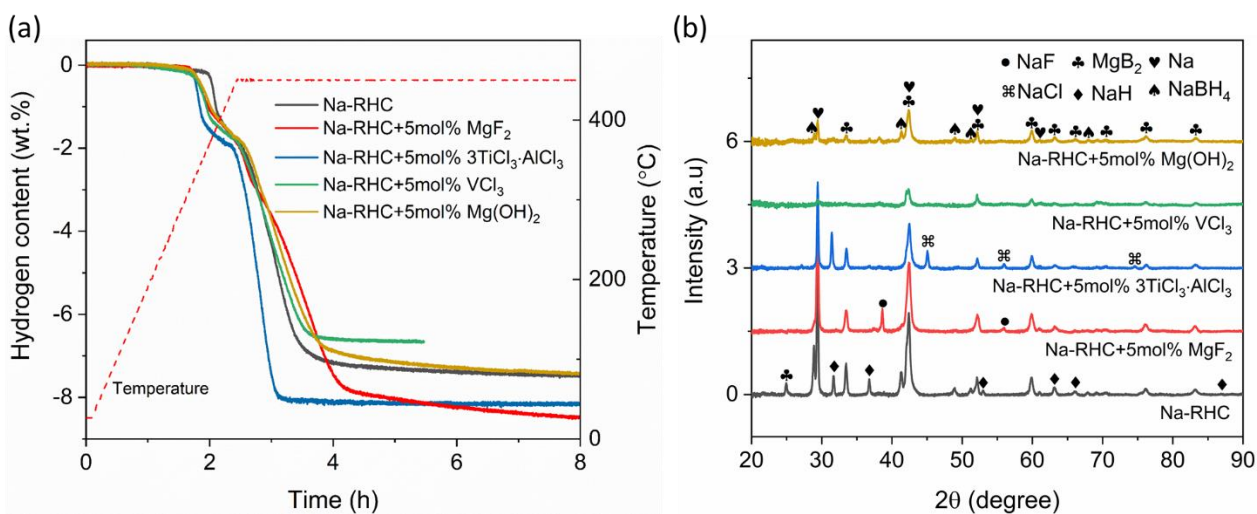**Fig. 2.** (a) Dehydrogenation curves and (b) corresponding XRD patterns after dehydrogenation of Na-RHC, Na-RHC + 5 mol% MgF_2, $3TiCl_3 \cdot AlCl_3$, VCl_3, and $Mg(OH)_2$ samples. The dehydrogenation measurements

were performed under 15 kPa backpressure while heating from room temperature to 450 °C with a heating rate of 3 °C/min and then kept isothermal at 450 °C for 5 to 8 hours.

3.3 Equilibrium phase compositions

In order to understand the reaction mechanism of the dehydrogenation process of the Na-RHCs with and without additives, the equilibrium phase composition calculations were performed by minimizing the Gibbs free energy via the HSC Chemistry software[63]. The calculated results are shown in Table 2. For the MgF_2, $3TiCl_3 \cdot AlCl_3$, and VCl_3 doped samples, NaCl and NaF were calculated to be the potential products, which is in good agreement with the XRD results shown in Fig. 2(b). According to the minimization of Gibbs free energy, the formation of TiB_2 and VB_2 is also possible during the dehydrogenation process, which is well suited to the reported TM-based borides characterized by TEM from literature[57,71-74]. These phases are not detected by XRD as shown in Fig. 2 (b). Hence, in the following section further structural characterizations are presented, revealing the presence of these species.

Table 2 The calculated equilibrium phase compositions of Na-RHC + 5 mol% MgF_2, $3TiCl_3 \cdot AlCl_3$, VCl_3, and $Mg(OH)_2$ after dehydrogenation. The calculations are based on the following conditions: from RT to 500 °C under 1 bar of H_2 pressure.

System	Dehydrogenation pathway
$1.8\ NaBH_{4(s)} + MgH_{2(s)}$	$1.8\ NaH_{(s)} + 0.1\ Mg_{(s)} + 0.90\ MgB_{2(s)} + 3.7\ H_{2(g)}$
$1.8\ NaBH_{4(s)} + MgH_{2(s)} + 0.015\ MgF_{2(s)}$	$1.77\ NaH_{(s)} + 0.115\ Mg_{(s)} + 0.03\ NaF_{(s)} + 0.90\ MgB_{2(s)} + 3.7150\ H_{2(g)}$
$1.865\ NaBH_{4(s)} + MgH_{2(S)} + 0.1125\ TiCl_{3(S)} + 0.0375\ AlCl_{3(S)}$	$1.415\ NaH_{(S)} + 0.0375\ Al_{(S)} + 0.18\ Mg_{(S)} + 0.45\ NaCl_{(S)} + 0.82\ MgB_{2(S)} + 0.1125\ TiB_{2(S)} + 4.0225\ H_{2(g)}$
$1.8\ NaBH_{4(s)} + MgH_{2(s)} + 0.015\ VCl_{3(s)}$	$1.755\ NaH_{(s)} + 0.115\ Mg_{(s)} + 0.045\ NaCl_{(s)} + 0.885\ MgB_{2(s)} + 0.015\ VB_{2(s)} + 3.7225\ H_{2(g)}$
$1.8\ NaBH_{4(s)} + MgH_{2(s)} + 0.015\ Mg(OH)_{2(s)}$	$1.8\ NaH_{(s)} + 0.085\ Mg_{(s)} + 0.03\ MgO_{(s)} + 0.90\ MgB_{2(s)} + 3.715\ H_{2(g)}$

3.4 Microstructural and Morphology properties

As previously mentioned, the addition of the TM-based additives influences the kinetic behavior of $2NaBH_4 + MgH_2$. Similar behaviors are generally observed also for the systems $2LiBH_4 + MgH_2$ and $Ca(BH_4)_2 + MgH_2$ doped with TM-based additives[51-55]. However, for the system $2NaBH_4 + MgH_2$, only the additive $3TiCl_3 \cdot AlCl_3$ appears to enhance the kinetic behavior

of the second dehydrogenation step. The use of additives prior to grinding frequently results in noticeable microstructural alterations. This is related to the formation of hard nanoparticles, which during milling improve the grain refinement process and, as a result, reduce the diffusion length distances in the system and the enlarged reactant contact area. For this reason, the crystallite sizes of $NaBH_4$ and MgH_2 after milling and of MgB_2 after dehydrogenation were calculated for all investigated samples (Table 3) by using the Scherrer formula on the related XRD peaks. On the one hand, the crystallite sizes of the $NaBH_4$ and MgH_2 vary from one additive to the other. In the case of the sample containing MgF_2, the crystallite sizes of the $NaBH_4$ and MgH_2 are 30.2 ± 1.5 nm and 21.2 ± 1.1 nm, respectively. While for the sample containing $3TiCl_3 \cdot AlCl_3$, crystallite sizes of the $NaBH_4$ and MgH_2 are 20.9 ± 1.0 nm and 15.7 ± 0.8 nm, respectively. On the other hand, the crystallite size values for MgB_2 in the desorbed materials are around 13 nm, thus independent of the presence of the additives.

Table 3 Crystallite size of $NaBH_4$ and MgH_2 in the milled and MgB_2 in the dehydrogenated Na-RHC + 5 mol% MgF_2, $3TiCl_3 \cdot AlCl_3$, VCl_3, and $Mg(OH)_2$ samples, as determined by using Scherrer formula on the related XRD peaks.

Composition	As milled		After dehydrogenation
	Crystallite size of $NaBH_4$ (nm)	Crystallite size of MgH_2 (nm)	Crystallite size of MgB_2 (nm)
Na-RHC	25.0 ± 1.3	16.6 ± 0.8	13.9 ± 0.7
Na-RHC + 5 mol% MgF_2	30.2 ± 1.5	21.2 ± 1.1	13.7 ± 0.7
Na-RHC + 5 mol% $3TiCl_3 \cdot AlCl_3$	20.9 ± 1.0	15.7 ± 0.8	14.3 ± 0.7
Na-RHC + 5 mol% VCl_3	22.7 ± 1.1	16.8 ± 0.8	12.9 ± 0.6
Na-RHC + 5 mol% $Mg(OH)_2$	26.0 ± 1.3	18.9 ± 0.9	13.7 ± 0.7

As the reaction rate for the second step is related to the nucleation and growth of MgB_2 particles[57], the morphology of the formed MgB_2 is investigated *via* different TEM techniques. Owing to the fastest achieved dehydrogenation kinetics, the sample selected for this investigation is the dehydrogenated Na-RHC doped with $3TiCl_3 \cdot AlCl_3$. Pure Na-RHC is used for comparison.

According to Fig. 3(a) and (b), the pure Na-RHC contains plate-shaped MgB_2. The plates are visible in bright contrast in Fig. 3(a). Higher magnification images suggest that these MgB_2 particles have most likely plate-like morphology, as shown in the high-angle annular dark-field (HAADF) image in Fig. 3(c) and the related diffraction pattern Fig. 3(d). The corresponding

energy-dispersive X-ray spectroscopy (EDX) mappings of different elements containing Na, Mg, and Cu are shown in Fig. 3(e)-(h). The results confirm the plate-like morphology of MgB_2, as revealed previously. Note that the existence of Cu originates from the use of the Cu grid for TEM measurements.
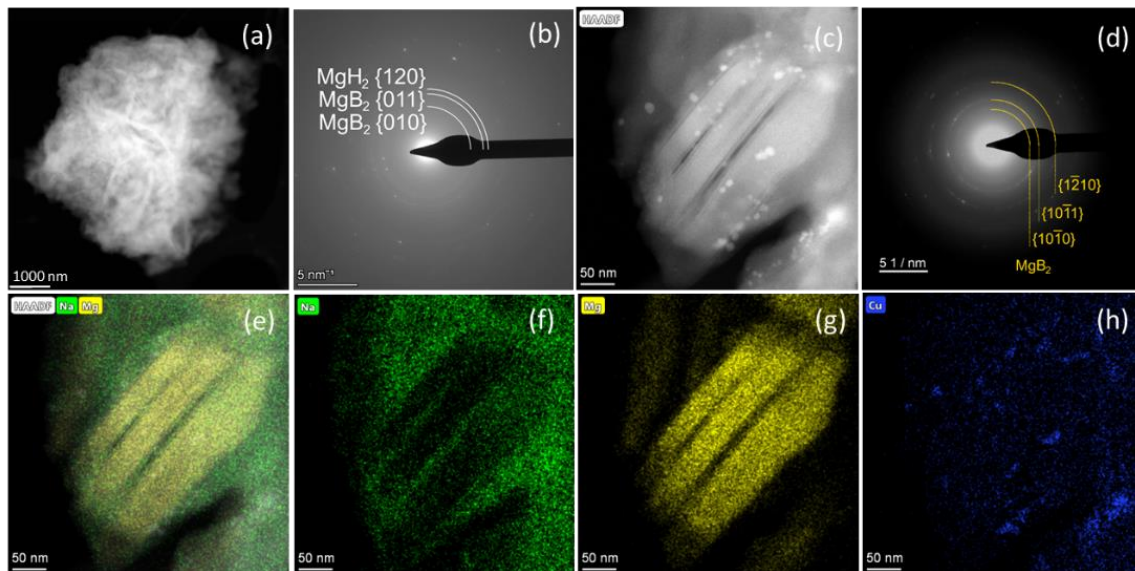
Fig. 3. (a) TEM and (b) the corresponding FFT images of the pure Na-RHC sample after dehydrogenation. (c)-(f) The corresponding EDX mapping of different elements, *e.g.*, Na, Mg, and Cu, for the area in (c).

Differently, as shown in Fig. 4(a) and (b), the MgB_2 particles in the sample doped with 5 mol% $3TiCl_3 \cdot AlCl_3$ are distributed more uniformly. The HAADF image in Fig. 4(c) illustrates a typical needle-like structure of MgB_2, in the 2D image. However, the 3D morphology has not been identified yet. We stay with the designation "needle" here because of its appearance in the 2D images. The corresponding electron energy loss spectroscopy (EELS) mapping data in Fig. 4(d) confirms the presence of several elements, *e.g.,* Mg, B, and Ti, for the area in Fig. 4(c), and the MgB_2 particles are surrounded by Ti-containing compounds. Except for MgB_2, the EDX mappings of Ti and B indicate that both overlap. Hence, this result suggests that nanostructured TiB_2 is present and results from the reaction between the additives and the starting materials.
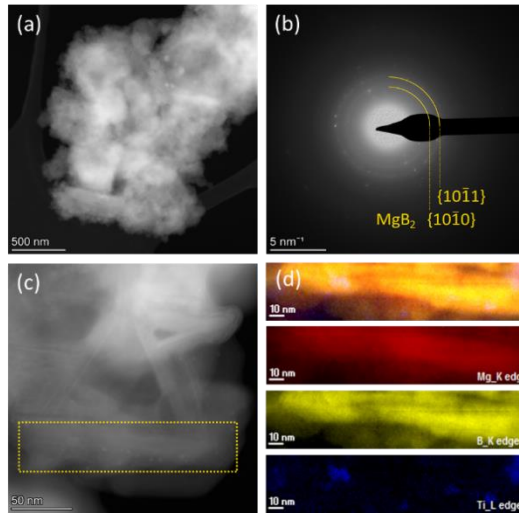
Fig. 4. (a) TEM and (b) the corresponding FFT images of the $2NaBH_4+MgH_2+5mol\%$ $3TiCl_3 \cdot AlCl_3$ sample after dehydrogenation. (c) Enlarged image of the area shown in (a). (d) The corresponding EELS mapping of different elements, including Mg, B, and Ti for (c). The crystallographic information of the rings on the diffraction pattern comes from the entire region in (a).

As can be seen in the HAADF image (Fig. 5(a)) and corresponding EDX mapping (Fig. 5(b)-(d)) of the formed MgB_2 for the sample doped with 5 mol% $3TiCl_3 \cdot AlCl_3$ after dehydrogenation, the needle-like structure presented in Fig. 5(a) is proved to be MgB_2. To further investigate the effects of $3TiCl_3 \cdot AlCl_3$ additive on the formation of MgB_2, HRTEM was used to verify the size and shape of the represented MgB_2 in the sample doped with 5 mol% $3TiCl_3 \cdot AlCl_3$. Fig 5(e), (f), and (g) show the areas that contain needle-like MgB_2 particles with a thickness of 10-20 nm, in different magnifications. Fig. 5(h) is the corresponding fast Fourier-transform (FFT) pattern of Fig. 5(g), which proves that the observed particles belong to the MgB_2 {0002} plane.
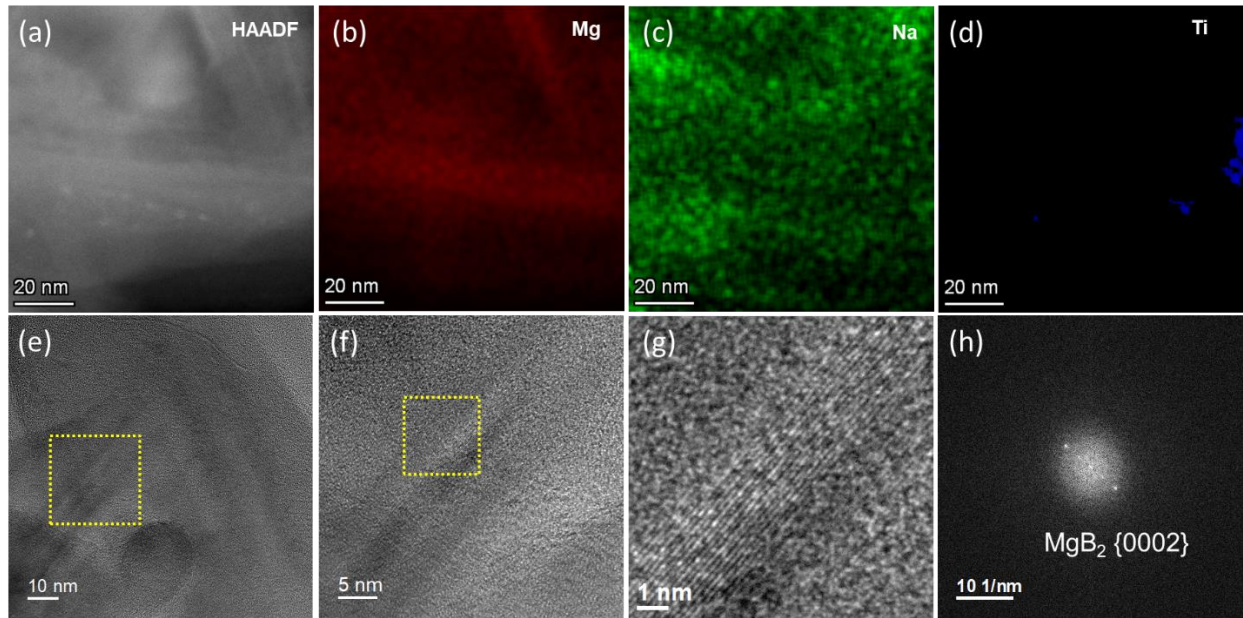
Fig. 5. (a) HAADF image and (b)-(d) corresponding Mg, Na, and Ti EDX mapping of the formed MgB_2 for the sample doped with 5 mol% $3TiCl_3 \cdot AlCl_3$ after dehydrogenation. (e) HRTEM image of the formed MgB_2. (f) The enlarged image of the selected area shown in (a). (g) The enlarged image of the selected area in (b). (h) The corresponding FFT profile of (g).

Fig. 6(a), (b), (c) and the fast Fourier-transform (FFT) pattern (d) confirm the formation of TiB_2 and/or AlB_2 (abbreviated with "/") from the $3TiCl_3 \cdot AlCl_3$ additive as suggested by the equilibrium phase compositions calculation (Table 1). The detected spherical TiB_2/AlB_2 nanoparticles appear in a size range between 1 and 5 nm. The corresponding FFT pattern of Fig. 6(c) proves that the particle orientation correlates with the [211] zone axis of TiB_2/AlB_2.
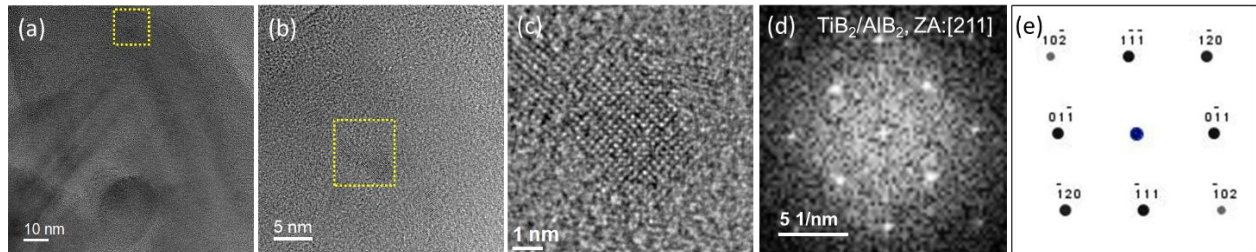

Fig. 6. (a) HRTEM images of the sample doped with 5 mol% $3TiCl_3 \cdot AlCl_3$ after dehydrogenation. (b) The enlarged image of the selected area shown in (a). (c) The enlarged image of the selected area in (b). (d) The corresponding FFT profile of (c). (e) The simulated diffraction pattern of TiB_2/AlB_2.

3.5 Size distribution of the boride additives

TEM investigation provided an insight into the morphology of the formed MgB_2 and the sizes

of the compounds formed by the interaction of the additives with the Na-RHC. In the following, it is investigated if these locally observed structures are evenly distributed in the samples. For this, SAXS analyses of the pure Na-RHC and Na-RHC + 5 mol% $3TiCl_3 \cdot AlCl_3$ after dehydrogenation were performed, and the results are reported in Fig. S11. Based on the results obtained by TEM, a cylindrical-shaped particle geometry for fitting the SAXS data concerning the MgB_2 particles has been applied. As shown in the fitting result (Fig. 7(a)), the MgB_2 particles in the dehydrogenated pure Na-RHC appear to have a mean diameter of 47 nm. In addition, the average length of these MgB_2 particles is 284 nm. Instead, for the dehydrogenated $3TiCl_3 \cdot AlCl_3$ doped sample, the average diameter and length of MgB_2 particles are reduced to 28.0 nm and 110 nm, respectively. Thus, the size of the MgB_2 particles in the sample with the $3TiCl_3 \cdot AlCl_3$ additive is 86 % smaller than for the pure Na-RHC. These SAXS measurements results show that the MgB_2 needle-like structures observed by TEM are not a local singularity since they are homogeneously distributed all over the sample. However, due to the range of dimensions investigated (100 nm), a description of the morphology of the MgB_2 particles larger than 100 nm cannot be given. Based on the TEM investigation, the average dimension of the TiB_2/AlB_2 falls in the range of few nanometers, *i.e.,* 1 − 5 nm (Fig. 6). While observing the SAXS spectra, we can see that, for the dehydrogenated $3TiCl_3 \cdot AlCl_3$ doped sample, some structures are present in the range between 1 and 5 nm and are well described by a spherical symmetry model, as shown in Fig. 7(b). The mean radius of these structures is 1.5 nm. Besides, bigger particles have a mean diameter of 7.2 nm. Therefore, the TiB_2/AlB_2 nanoparticle structures observed in the TEM analyses are supported by SAXS outcomes.
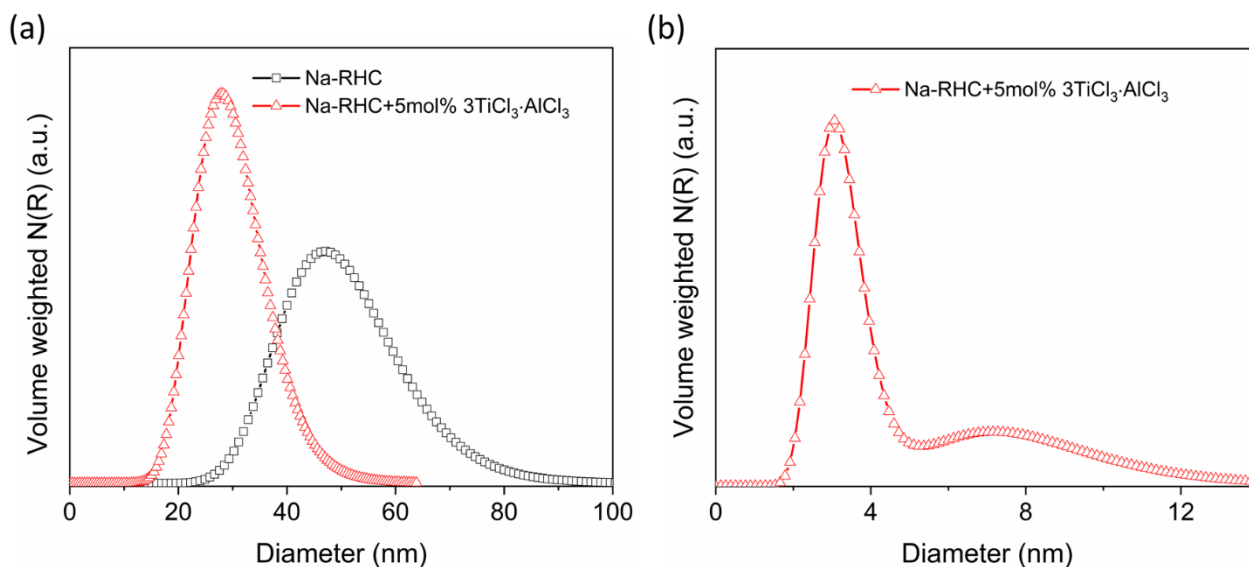

Fig. 7. (a) Size distribution of MgB_2 particles in dehydrogenated pure Na-RHC and Na-RHC + 5 mol%

3TiCl$_3$·AlCl$_3$ samples. (b) Size distribution of TiB$_2$/AlB$_2$ in dehydrogenated Na-RHC + 5 mol% 3TiCl$_3$·AlCl$_3$ sample. Note the different scale for the diameters in (a) and (b).

3.6 Kinetic modeling

In order to understand the effects of additives on the dehydrogenation of NaBH$_4$ and nucleation of MgB$_2$, the rate-limiting mechanism was evaluated using the Sharp and Jones method[67,68]. The analyses were carried out for the second step of the dehydrogenation reactions since it covers about 80 % of the hydrogen release and is slower. The reacted fractions considered for that are 0.1 − 0.7 (for pure Na-RHC) and 0.1 − 0.8 (for Na-RHC + 5 mol% 3TiCl$_3$·AlCl$_3$) as shown in Fig. S12. Note that the reaction fraction of 0.1 − 0.7 and 0.1 − 0.8 is the fraction of the second dehydrogenation process, which means that the initial values of the overall reaction (the first plus the second dehydrogenation process) are 0.34 − 0.78 and 0.33 − 0.85, respectively. The results of the pristine sample and the one doped with 3TiCl$_3$·AlCl$_3$ can be seen in Table 4, whereas the corresponding fitting parameters can be seen in Fig. S13 and Table S12-13. For the pure Na-RHC, the rate-limiting step is two-dimensional interface controlled (R2), indicating that the reaction is controlled by the interface movements toward the center of the crystal[75]. For the sample doped with 5 mol% 3TiCl$_3$·AlCl$_3$, the rate-limiting step changes to the F2 Johnson-Mehl-Avrami (JMA) model. The main limiting factor is random nucleation with one-dimensional diffusion having a constant number of nuclei (F2)[76,77], The original and fitting curves by R2 and F2 models of these two samples are shown in Fig. 8. We suggest that the reaction kinetics depends markedly on the number and type of nucleation sites present in the system, defining the diffusion lengths. However, the proposed fitts are not fully satisfactory in particular for what concerns the pure Na-RHC. Although to give an accurate description of the reasons for the observed divergences is not easy, a careful analysis of what is already known about this system might help. In his PhD dissertation, one of the coauthors of this manuscript[78] reported on the formation of a NaH-NaBH$_4$ molten phase during the dehydrogenation of the system 2NaBH$_4$+MgH$_2$ for temperature higher than 380 °C. Thus, the second step of dehydrogenation of 2NaBH$_4$+MgH$_2$ starts with an interaction between solid NaBH$_4$ and Mg to form NaH and MgB$_2$. However, as soon as NaH is available, it interacts with a portion of the still present NaBH$_4$ to form a NaH-NaBH$_4$ molten phase. At this point, the formation of the products Na/NaH+MgB$_2$ might follow multiple competing paths, *i.e.* by the interaction of the NaH-NaBH$_4$ molten phase with Mg or by the interaction of the remaining solid NaBH$_4$ with Mg. Thus, the discrepancies between the experimental data and the kinetic fitting

might arise from the fact that the reaction mechanisms at the base of the second dehydrogenation step of the system $2NaBH_4+MgH_2$ are multiple and occur simultaneously in a competitive manner.

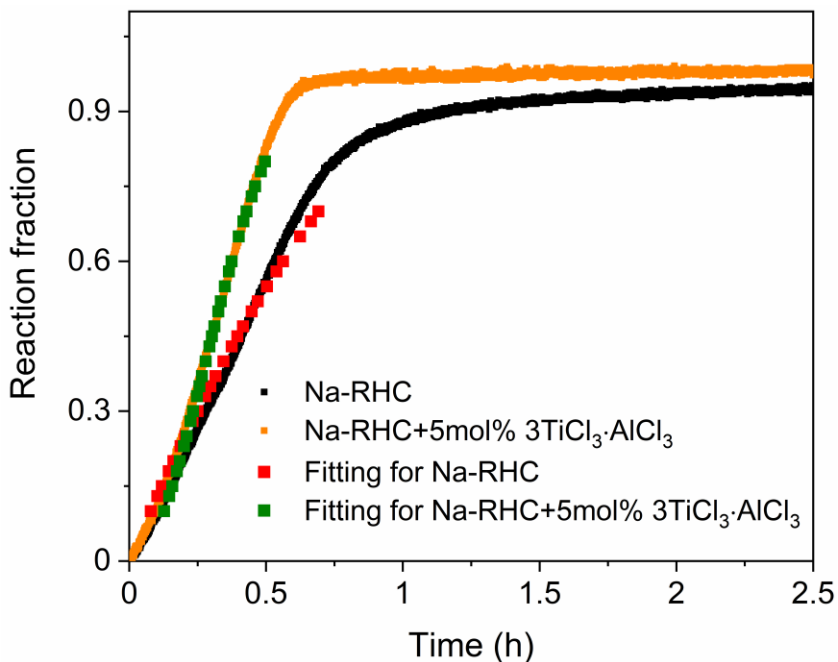**Fig. 8.** Reaction fraction versus time plots for the pure Na-RHC and Na-RHC + 5 mol% $3TiCl_3 \cdot AlCl_3$ samples, the fitting curves of R2 model for pure Na-RHC and F2 model for Na-RHC + 5 mol% $3TiCl_3 \cdot AlCl_3$ are also shown.

Table 4 Kinetic models for dehydrogenation of Na-RHC and Na-RHC + 5 mol% $3TiCl_3 \cdot AlCl_3$.

Composition	Kinetic model	Rate-limiting mechanism
Na-RHC	R2	Two-dimensional interface controlled
Na-RHC + 5mol% $3TiCl_3 \cdot AlCl_3$	F2	Random nucleation with one-dimensional diffusion having a constant number of nuclei

3.7 Role of additives on the reaction kinetics and morphology

Compared to the pure Na-RHC, adding 5 mol% of $3TiCl_3 \cdot AlCl_3$ (Fig. 2(a)) markedly improves the dehydrogenation kinetics of Na-RHC + 5 mol% $3TiCl_3 \cdot AlCl_3$ and significantly modifies the MgB_2 particle morphology. The possible reasons lying behind such changes are discussed in the following.

Firstly, the smaller particle size of MgB_2 in the doped sample (Fig. 7(a)), 86% smaller than

in the pure sample, leads to an increase in the surface area of MgB_2. Such an increase in surface area of MgB_2 is an essential factor during dehydrogenation because an increased number of nucleation sites of these smaller MgB_2 structures might lead to smaller diffusion distances for the B- and Mg-carrying species. Thus the change in morphology of MgB_2 can promote the reaction rate[74,79]. The enhancement of the dehydrogenation rate of the $3TiCl_3 \cdot AlCl_3$ doped samples is related to a faster formation of MgB_2. In this regard, the formed TiB_2/AlB_2 nanoparticles might act as additional nucleation centers[60] for MgB_2. However, evaluating if the TiB_2/AlB_2 nanoparticles are suitable nucleation centers for MgB_2, parameters such as interatomic and planar mismatches should be considered. In fact, when interatomic and planar mismatches between the parental and the nucleating phase are low, the elastic strain energy in the newly forming phase is low, and the nucleation process is favored. The minimum interfacial energy between adjacent phases is usually achieved by matching the close-packed or nearly close-packed planes. Based on the edge-to-edge model[61], a good matching orientation relationship should fulfill the criteria that its interatomic mismatch and interplanar mismatches are less than 10% and 6%, respectively[59,61].

Therefore, the interatomic and planar mismatches being important quantities to understand the role of the additives on the dehydrogenation behavior of Na-RHC, these values were calculated for several phases related to the nucleation of MgB_2 in the pure and the $3TiCl_3 \cdot AlCl_3$ doped system. As reported in Table 5, the calculated interatomic mismatch between MgB_2 and TiB_2/AlB_2 (1.74% for $<11\text{-}20>MgB_2 \parallel <11\text{-}20> TiB_2$ and 2.53% for $<11\text{-}20>MgB_2 \parallel <11\text{-}20> AlB_2$) is smaller than that between MgB_2 and Mg (2.54% for $<10\text{-}10>MgB_2 \parallel <0001>Mg$. In addition, The interplanar mismatch between MgB_2 and TiB_2 (1.74% for $\{10\text{-}10\}MgB_2 \parallel \{10\text{-}10\}TiB_2$) is smaller than the mismatch between MgB_2 and Mg (2.55% for $\{10\text{-}10\}MgB_2 \parallel \{0001\}Mg$), and the mismatch between MgB_2 and AlB_2 is 2.67% (for $\{10\text{-}10\}MgB_2 \parallel \{10\text{-}10\}AlB_2$). Thus, the smaller interatomic and interplanar mismatches between MgB_2 and TiB_2/AlB_2 are expected to provide a kinetically favored path for the nucleation of MgB_2 in the $3TiCl_3 \cdot AlCl_3$ doped system compared to the pure system. Furthermore, the Na-RHC + 5 mol% $3TiCl_3 \cdot AlCl_3$ material presents a refined MgB_2 microstructure and a homogenous distribution of needle-like MgB_2 and spherical-like transition metal borides (Sections 3.4 and 3.5). Hence, the suitable interatomic and interplanar mismatches between MgB_2 and TiB_2/AlB_2, the refined microstructure, and the homogenous distribution of nuclei sites enhance the interphase nucleation avoiding the interphase controlled mechanism. Thus, faster dehydrogenation kinetics can be observed in Fig. 2(a).

Table 5 Calculated interatomic and interplanar mismatch between MgB_2 and several possible phases.

Composition	Matching directions	Interatomic mismatch (%)	Matching planes	Interplanar mismatch (%)
TiB$_2$	<11-20>MgB$_2$ || <11-20> TiB$_2$	1.74	{10-10}MgB$_2$ || {10-10}TiB$_2$	1.74
AlB$_2$	<11-20>MgB$_2$ || <11-20> AlB$_2$	2.53	{10-10}MgB$_2$ || {10-10}AlB$_2$	2.67
Mg	<10-10>MgB$_2$ || <0001>Mg	2.54	{10-10}MgB$_2$ || {0001}Mg	2.55

The TEM analyses reported in Fig. 3 and 4 showed that the MgB$_2$ in the pristine Na-RHC has a plate-like structure, whereas the 3TiCl$_3$·AlCl$_3$ doped sample has a needle-like structure. These results are well in agreement with the work of Lee *et al.*[80] and Jin *et al.*[60]. In fact, in their work, Lee *et al.* claimed that the growth of MgB$_2$ crystal takes place preferentially in two dimensions, while the growth on the third (i.e., *c*-axis [0002]) is hindered, leading to MgB$_2$ morphologies similar to those observed in this work, *e.g.*, plate-like and needle-like. The produced MgB$_2$ in both samples may have a needle-like shape. However, in the undoped sample, MgB$_2$ growth occurs on a parental phase (*i.e.*, Mg) with a diameter of several micrometers (Fig. 7(a)), which could result in side-by-side clustering of many needles in a particular direction. On the contrary, in the doped samples, the parental phases (*e.g.*, TiB$_2$/AlB$_2$) have a particle dimension of few nm that does not allow for the formation of multiple needles and their clustering. Thus, the needles appear as single entities randomly oriented.

4. Conclusions

In this work, the effects of the TM-based additives, *i.e.*, MgF$_2$, 3TiCl$_3$·AlCl$_3$, VCl$_3$, and Mg(OH)$_2$ on the dehydrogenation kinetics of the 2NaBH$_4$ + MgH$_2$ system were investigated. The conclusions are as follows:

(1) The 3TiCl$_3$·AlCl$_3$ doped sample shows the fastest dehydrogenation kinetics, *e.g.,* 8.0 wt.% of hydrogen can be released in 3 hours.

(2) Equilibrium phase composition calculations show that TiB$_2$/AlB$_2$ particles can be formed after dehydrogenation, verified by TEM analyses.

(3) The MgB$_2$ in the doped sample exhibits a needle-like structure, as observed by 2D images, which differs from the plate-like structure of the un-doped sample.

(4) Rate-limiting mechanism of the second step of the dehydrogenation reaction shows that the addition of 3AlCl$_3$·AlCl$_3$ changes the reaction mechanism from a two-dimensional interface

controlled reaction to random nucleation with one-dimensional diffusion having a constant number of nuclei. Therefore, the *in-situ* formed transition nanostructured metal borides and the refined needle-like shape of MgB_2 accelerate the interface controlled mechanism of the MgB_2 nuclei formation upon dehydrogenation. The reasons why the combination of the *in-situ* formed nanostructured metal borides and the refined needle-like shape of MgB_2 improve the dehydrogenation kinetic behavior of Na-RHC can be attributed to: First, the additives disperse the particles of $NaBH_4$ and MgH_2 more homogenously, which offers more nucleation sites for MgB_2. Second, a smaller misfit between MgB_2 and TiB_2/AlB_2 is expected to weaken the nucleation barrier, thus promoting the reaction rate.
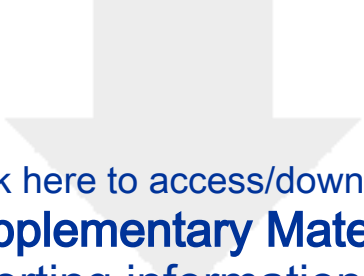
Acknowledgments

References

1   Dunn, S. On hydrogen futures: toward a sustainable energy system - Author's reply. *Int J Hydrogen Energ* **28**, 135-135(2003).

2   Winter, C. J. Hydrogen energy - Abundant, efficient, clean: A debate over the energy-system-of-change. *Int J Hydrogen Energ* **34**, S1-S52(2009).

3   Momirlan, M. & Veziroglu, T. N. Current status of hydrogen energy. *Renew Sust Energ Rev* **6**, 141-179(2002).

4   Pistidda, C. Solid-State Hydrogen Storage for a Decarbonized Society. *Hydrogen* **2**, 428-443(2021).

5   Tzimas, E., Filiou, C., Peteves, S. & Veyret, J. B. HYDROGEN STORAGE: STATE-OF-THE-ART AND FUTURE PERSPECTIVE. (2003).

6   Hoogers, G. *Fuel cell technology handbook*. (CRC press, 2002).

7   Zecevic, S., Patton, E. M. & Parharni, P. Carbon-air fuel cell without a reforming process. *Carbon* **42**, 1983-1993(2004).

8   Hayes, M. D., Xin, H., Li, H., Shepherd, T. A. & Stinn, J. P. Electricity and Fuel Use of Aviary-Laying Hen Houses in the Midwestern United States. *Appl Eng Agric* **30**, 259-266(2014).

9   Jensen, J. O., Vestbo, A. P., Li, Q. & Bjerrum, N. J. The energy efficiency of onboard hydrogen storage. *J Alloy Compd* **446**, 723-728(2007).

10   Milanese, C., Garroni, S., Gennari, F., Marini, A., Klassen, T., Dornheim, M. & Pistidda, C. Solid State Hydrogen Storage in Alanates and Alanate-Based Compounds: A Review. *Metals-Basel* **8**(2018).

11   Milanese, C., Jensen, T. R., Hauback, B. C., Pistidda, C., Dornheim, M., Yang, H., Lombardo, L., Zuettel, A., Filinchuk, Y., Ngene, P., de Jongh, P. E., Buckley, C. E., Dematteis, E. M. & Baricco, M. Complex hydrides for energy storage. *International Journal of Hydrogen Energy* **44**, 7860-7874(2019).

12   Capurso, G., Schiavo, B., Jepsen, J., Lozano, G. A., Metz, O., Klassen, T. & Dornheim, M. Metal Hydride-Based Hydrogen Storage Tank Coupled with an Urban Concept Fuel Cell Vehicle: Off Board Tests. *Adv Sustain Syst* **2**(2018).

13   Schneemann, A., White, J. L., Kang, S., Jeong, S., Wan, L. W. F., Cho, E. S., Heo, T. W., Prendergast, D., Urban, J. J., Wood, B. C., Allendorf, M. D. & Stavila, V. Nanostructured Metal Hydrides for Hydrogen Storage. *Chem Rev* **118**, 10775-10839(2018).

14   Schlapbach, L. & Zuttel, A. Hydrogen-storage materials for mobile applications. *Nature* **414**, 353-358(2001).

15   Dillon, A. C., Jones, K. M., Bekkedahl, T. A., Kiang, C. H., Bethune, D. S. & Heben, M. J. Storage of hydrogen in single-walled carbon nanotubes. *Nature* **386**, 377-379(1997).

16   Ley, M. B., Jepsen, L. H., Lee, Y. S., Cho, Y. W., von Colbe, J. M. B., Dornheim, M., Rokni, M., Jensen, J. O., Sloth, M., Filinchuk, Y., Jorgensen, J. E., Besenbacher, F. & Jensen, T. R. Complex hydrides for hydrogen storage - new perspectives. *Materials Today* **17**, 122-128(2014).

17   Pistidda, C., Barkhordarian, G., Rzeszutek, A., Garroni, S., Minella, C. B., Baro, M. D., Nolis, P., Bormann, R., Klassen, T. & Dornheim, M. Activation of the reactive hydride composite 2NaBH(4) + MgH2. *Scripta Mater* **64**, 1035-1038(2011).

18   Bosenberg, U., Ravnsbaek, D. B., Hagemann, H., D'Anna, V., Minella, C. B., Pistidda, C., van Beek, W., Jensen, T. R., Bormann, R. & Dornheim, M. Pressure and Temperature Influence on the Desorption Pathway of the LiBH4-MgH2 Composite System. *J Phys Chem C* **114**, 15212-15217(2010).

19   Pistidda, C., Bergemann, N., Wurr, J., Rzeszutek, A., Moller, K. T., Hansen, B. R. S., Garroni, S., Horstmann, C., Milanese, C., Girella, A., Metz, O., Taube, K., Jensen, T. R., Thomas, D., Liermann, H. P., Klassen, T. & Dornheim, M. Hydrogen storage systems from waste Mg alloys. *J Power Sources* **270**, 554-563(2014).

20   Dematteis, E. M., Berti, N., Cuevas, F., Latroche, M. & Baricco, M. Substitutional effects in TiFe for hydrogen storage: a comprehensive review. *Mater Adv*(2021).

21   Wang, H., Wu, G. T., Cao, H. J., Pistidda, C., Chaudhary, A. L., Garroni, S., Dornheim, M. & Chen, P. Near Ambient Condition Hydrogen Storage in a Synergized Tricomponent Hydride System. *Adv Energy Mater* **7**(2017).

22   Mueller, W. M., Blackledge, J. P. & Libowitz, G. G. *Metal hydrides*. (Elsevier, 2013).

23   Orimo, S. I., Nakamori, Y., Eliseo, J. R., Zuttel, A. & Jensen, C. M. Complex hydrides for hydrogen storage. *Chem Rev* **107**, 4111-4132(2007).

24   Orimo, S., Nakamori, Y., Kitahara, G., Miwa, K., Ohba, N., Towata, S. & Zuttel, A. Dehydriding and rehydriding reactions of LiBH4. *J Alloy Compd* **404**, 427-430(2005).

25   Yadav, M. & Xu, Q. Liquid-phase chemical hydrogen storage materials. *Energ Environ Sci* **5**, 9698-9725(2012).

26   Bogdanovic, B. & Schwickardi, M. Ti-doped alkali metal aluminium hydrides as potential novel reversible hydrogen storage materials. *J Alloy Compd* **253**, 1-9(1997).

27   Hagemann, H. Boron Hydrogen Compounds: Hydrogen Storage and Battery Applications. *Molecules* **26**(2021).

28   Hagemann, H. Estimation of Thermodynamic Properties of Metal Hydroborates. *Chemistryselect* **4**, 8989-8992(2019).

29   Barkhordarian, G., Klassen, T. & Bormann, R. Metal-containing hydrogen-storing material and its production. *PCT International Application*(2005).

30   Vajo, J., Mertens, F. O., Skeith, S. & Balogh, M. P. Reversible hydrogen storage system using hydride mixture. *PCT International Application*(2005).
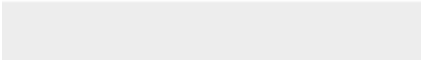
31 Dornheim, M., Doppiu, S., Barkhordarian, G., Boesenberg, U., Klassen, T., Gutfleisch, O. & Bormann, R. Hydrogen storage in magnesium-based hydrides and hydride composites. *Scripta Mater* **56**, 841-846(2007).

32 Vajo, J. J. & Olson, G. L. Hydrogen storage in destabilized chemical systems. *Scripta Mater* **56**, 829-834(2007).

33 Sudik, A., Yang, J., Siegel, D. J., Wolverton, C., Carter, R. O. & Drews, A. R. Impact of Stoichiometry on the Hydrogen Storage Properties of LiNH2-LiBH4-MgH2 Ternary Composites. *J Phys Chem C* **113**, 2004-2013(2009).

34 Yang, J., Sudik, A., Siegel, D. J., Halliday, D., Drews, A., Carter, R. O., Wolverton, C., Lewis, G. J., Sachtler, J. W. A., Low, J. J., Faheem, S. A., Lesch, D. A. & Ozolins, V. Hydrogen storage properties of 2LiNH(2)+ LiBH4+MgH2. *J Alloy Compd* **446**, 345-349(2007).

35 Barkhordarian, G., Klassen, T., Dornheim, M. & Bormann, R. Unexpected kinetic effect of MgB2 in reactive hydride composites containing complex borohydrides. *J Alloy Compd* **440**, L18-L21(2007).

36 Garroni, S., Minella, C. B., Pottmaier, D., Pistidda, C., Milanese, C., Marini, A., Enzo, S., Mulas, G., Dornheim, M., Baricco, M., Gutfleisch, O., Suriñach, S. & Baró, M. D. Mechanochemical synthesis of NaBH4 starting from NaH-MgB 2 reactive hydride composite system. *Int J Hydrogen Energ* **38**, 2363-2369(2013).

37 Garroni, S., Pistidda, C., Brunelli, M., Vaughan, G. B. M., Suriñach, S. & Baró, M. D. Hydrogen desorption mechanism of 2NaBH4 + MgH2 composite prepared by high-energy ball milling. *Scripta Mater* **60**, 1129-1132(2009).

38 Nwakwuo, C. C., Pistidda, C., Dornheim, M., Hutchison, J. L. & Sykes, J. M. Microstructural analysis of hydrogen absorption in 2NaH + MgB2. *Scripta Mater* **64**, 351-354(2011).

39 Nwakwuo, C. C., Pistidda, C., Dornheim, M., Hutchison, J. L. & Sykes, J. M. Microstructural study of hydrogen desorption in 2NaBH4 + MgH2 reactive hydride composite. *Int J Hydrogen Energ* **37**, 2382-2387(2012).

40 Pistidda, C., Garroni, S., Minella, C. B., Dolci, F., Jensen, T. R., Nolis, P., Bösenberg, U., Cerenius, Y., Lohstroh, W., Fichtner, M., Baró, M. D., Bormann, R. & Dornheim, M. Pressure effect on the 2NaH + MgB2 hydrogen absorption reaction. *J Phys Chem C* **114**, 21816-21823(2010).

41 Pistidda, C., Napolitano, E., Pottmaier, D., Dornheim, M., Klassen, T., Baricco, M. & Enzo, S. Structural study of a new B-rich phase obtained by partial hydrogenation of 2NaH + MgB2. *Int J Hydrogen Energ* **38**, 10479-10484(2013).

42 Pistidda, C., Pottmaier, D., Karimi, F., Garroni, S., Rzeszutek, A., Tolkiehn, M., Fichtner, M., Lohstroh, W., Baricco, M., Klassen, T. & Dornheim, M. Effect of NaH/MgB2 ratio on the hydrogen absorption kinetics of the system NaH + MgB2. *Int J Hydrogen Energ* **39**, 5030-5036(2014).

43 Pottmaier, D., Pistidda, C., Groppo, E., Bordiga, S., Spoto, G., Dornheim, M. & Baricco, M. Dehydrogenation reactions of 2NaBH4 + MgH2 system. *Int J Hydrogen Energ* **36**, 7891-7896(2011).

44 Mao, J. F., Yu, X. B., Guo, Z. P., Liu, H. K., Wu, Z. & Ni, J. Enhanced hydrogen storage performances of NaBH4-MgH2 system. *J Alloy Compd* **479**, 619-623(2009).

45 Pistidda, C., Barkhordarian, G., Rzeszutek, A., Garroni, S., Minella, C. B., Baró, M., Nolis, P., Bormann, R., Klassen, T. & Dornheim, M. Activation of the reactive hydride composite 2NaBH4+ MgH2. *Scripta Mater* **64**, 1035-1038(2011).

46 Garroni, S., Milanese, C., Girella, A., Marini, A., Mulas, G., Menendez, E., Pistidda, C., Dornheim, M., Surinach, S. & Baro, M. D. Sorption properties of NaBH4/MH2 (M = Mg, Ti) powder systems. *Int J Hydrogen Energ* **35**, 5434-5441(2010).

47 Stasinevich, D., Egorenko, G. & Gnedina, G. in *Dokl. Akad. Nauk SSSR.* 610-612.

48 Garroni, S., Milanese, C., Pottmaier, D., Mulas, G., Nolis, P., Girella, A., Caputo, R., Olid, D., Teixdor, F., Baricco, M., Marini, A., Surinach, S. & Baro, M. D. Experimental Evidence of Na-

2[B12H12] and Na Formation in the Desorption Pathway of the 2NaBH(4) + MgH2 System. *J Phys Chem C* **115**, 16664-16671(2011).

49   Urgnani, J., Torres, F. J., Palumbo, M. & Baricco, M. Hydrogen release from solid state NaBH4. *Int J Hydrogen Energ* **33**, 3111-3115(2008).

50   Linstorm, P. NIST chemistry webbook, NIST standard reference database number 69. *J. Phys. Chem. Ref. Data, Monograph* **9**, 1-1951(1998).

51   Minella, C. B., Pistidda, C., Garroni, S., Nolis, P., Baró, M. D., Gutfleisch, O., Klassen, T., Bormann, R. & Dornheim, M. Ca(BH4)2 + MgH2: Desorption reaction and role of Mg on its reversibility. *J Phys Chem C* **117**, 3846-3852(2013).

52   Deprez, E., Justo, A., Rojas, T. C., López-Cartés, C., Bonatto Minella, C., Bösenberg, U., Dornheim, M., Bormann, R. & Fernández, A. Microstructural study of the LiBH4-MgH2 reactive hydride composite with and without Ti-isopropoxide additive. *Acta Mater* **58**, 5683-5694(2010).

53   Bonatto Minella, C., Pellicer, E., Rossinyol, E., Karimi, F., Pistidda, C., Garroni, S., Milanese, C., Nolis, P., Baró, M. D., Gutfleisch, O., Pranzas, K. P., Schreyer, A., Klassen, T., Bormann, R. & Dornheim, M. Chemical state, distribution, and role of Ti- and Nb-based additives on the Ca(BH4)2 system. *J Phys Chem C* **117**, 4394-4403(2013).

54   Bonatto Minella, C., Garroni, S., Pistidda, C., Gosalawit-Utke, R., Barkhordarian, G., Rongeat, C., Lindemann, I., Gutfleisch, O., Jensen, T. R., Cerenius, Y., Christensen, J., Baró, M. D., Bormann, R., Klassen, T. & Dornheim, M. Effect of transition metal fluorides on the sorption properties and reversible formation of Ca(BH4)2. *J Phys Chem C* **115**, 2497-2504(2011).

55   Bonatto Minella, C., Garroni, S., Pistidda, C., Baró, M. D., Gutfleisch, O., Klassen, T. & Dornheim, M. Sorption properties and reversibility of Ti(IV) and Nb(V)-fluoride doped-Ca(BH4)2-MgH2 system. *J Alloy Compd* **622**, 989-994(2015).

56   Bosenberg, U., Doppiu, S., Mosegaard, L., Barkhordarian, G., Eigen, N., Borgschulte, A., Jensen, T. R., Cerenius, Y., Gutfleisch, O., Klassen, T., Dornheim, M. & Bormann, R. Hydrogen sorption properties of MgH2-LiBH4 composites. *Acta Mater* **55**, 3951-3958(2007).

57   Bosenberg, U., Kim, J. W., Gosslar, D., Eigen, N., Jensen, T. R., von Colbe, J. M. B., Zhou, Y., Dahms, M., Kim, D. H., Gunther, R., Cho, Y. W., Oh, K. H., Klassen, T., Bormann, R. & Dornheim, M. Role of additives in LiBH4-MgH2 reactive hydride composites for sorption kinetics. *Acta Mater* **58**, 3381-3389(2010).

58   Karimi, F., Pranzas, P. K., Pistidda, C., Puszkiel, J. A., Milanese, C., Vainio, U., Paskevicius, M., Emmler, T., Santoru, A., Utke, R., Tolkiehn, M., Minella, C. B., Chaudhary, A. L., Boerries, S., Buckley, C. E., Enzo, S., Schreyer, A., Klassen, T. & Dornheim, M. Structural and kinetic investigation of the hydride composite Ca(BH4)(2) + MgH2 system doped with NbF5 for solid-state hydrogen storage. *Physical Chemistry Chemical Physics* **17**, 27328-27342(2015).

59   Zhang, M. X., Kelly, P. M., Easton, M. A. & Taylor, J. A. Crystallographic study of grain refinement in aluminum alloys using the edge-to-edge matching model. *Acta Mater* **53**, 1427-1438(2005).

60   Jin, O., Shang, Y., Huang, X., Mu, X., Szabó, D. V., Le, T. T., Wagner, S., Kübel, C., Pistidda, C. & Pundt, A. Microstructural Study of MgB2 in the LiBH4-MgH2 Composite by Using TEM. *Nanomaterials* **12**, 1893(2022).

61   Kelly, P. M. & Zhang, M. X. Edge-to-edge matching - The fundamentals. *Metall Mater Trans A* **37a**, 833-839(2006).

62   Cullity, B. D. Elements of X-Ray Diffraction. *American Journal of Physics* **25**, 394-395(1957).

63   Roine, A. HSC Chemistry for Windows—Chemical Reaction and Equilibrium Software with Extensive Thermochemical Database. *Outokumpu, HSC chemistry for Windows—Chemical ReOutokumpu Research Oy. Pori*(1999).

64   Bouamrane, A., de Brauer, C., Soulie, J. P., Letoffe, J. M. & Bastide, J. P. Standard enthalpies of formation of sodium-magnesium hydride and hydridofluorides NaMgH3, NaMgH2F and NaMgF2H. *Thermochim Acta* **326**, 37-41(1999).

65   Bouhadda, Y., Fenineche, N. & Boudouma, Y. Hydrogen storage: Lattice dynamics of orthorhombic NaMgH3. *Physica B* **406**, 1000-1003(2011).

66   Pottmaier, D., Pinatel, E. R., Vitillo, J. G., Garroni, S., Orlova, M., Baro, M. D., Vaughan, G. B. M., Fichtner, M., Lohstroh, W. & Baricco, M. Structure and Thermodynamic Properties of the NaMgH3 Perovskite: A Comprehensive Study. *Chem Mater* **23**, 2317-2326(2011).

67   Sharp, J. H., Brindley, G. W. & Achar, B. N. N. Numerical Data for Some Commonly Used Solid State Reaction Equations. *J Am Ceram Soc* **49**, 379-&(1966).

68   Jones, L. F., Dollimore, D. & Nicklin, T. Comparison of Experimental Kinetic Decomposition Data with Master Data Using a Linear Plot Method. *Thermochim Acta* **13**, 240-245(1975).

69   Mao, J. F., Gu, Q. F., Guo, Z. P. & Liu, H. K. Sodium borohydride hydrazinates: synthesis, crystal structures, and thermal decomposition behavior. *J Mater Chem A* **3**, 11269-11276(2015).

70   Ouyang, L. Z., Chen, W., Liu, J. W., Felderhoff, M., Wang, H. & Zhu, M. Enhancing the Regeneration Process of Consumed NaBH4 for Hydrogen Storage. *Adv Energy Mater* **7**(2017).

71   Fan, M. Q., Sun, L. X., Zhang, Y., Xu, F., Zhang, J. & Chu, H. L. The catalytic effect of additive Nb2O5 on the reversible hydrogen storage performances of LiBH4-MgH2 composite. *Int J Hydrogen Energ* **33**, 74-80(2008).

72   Deprez, E., Justo, A., Rojas, T. C., Lopez-Cartes, C., Minella, C. B., Bosenberg, U., Dornheim, M., Borrnann, R. & Fernandez, A. Microstructural study of the LiBH4-MgH2 reactive hydride composite with and without Ti-isopropoxide additive. *Acta Mater* **58**, 5683-5694(2010).

73   Wang, P. J., Ma, L. P., Fang, Z. Z., Kang, X. D. & Wang, P. Improved hydrogen storage property of Li-Mg-B-H system by milling with titanium trifluoride. *Energ Environ Sci* **2**, 120-123(2009).

74   Le, T.-T., Pistidda, C., Puszkiel, J. n., Castro Riglos, M. a. V., Karimi, F., Skibsted, J., GharibDoust, S. P., Richter, B., Emmler, T. & Milanese, C. Design of a nanometric AlTi additive for MgB2-based reactive hydride composites with superior kinetic properties. *The Journal of Physical Chemistry C* **122**, 7642-7655(2018).

75   Khawam, A. & Flanagan, D. R. Solid-state kinetic models: Basics and mathematical fundamentals. *J Phys Chem B* **110**, 17315-17328(2006).

76   Puszkiel, J. A. in *Gold nanoparticles-reaching new heights*   (IntechOpen London, UK, 2018).

77   Christian, J. W. *The theory of transformations in metals and alloys*. (Newnes, 2002).

78   Pistidda, C. *Hydrogen sorption properties of the composite system 2NaBH4+ MgH2*, Technische Universität Hamburg, (2011).

79   Shang, Y. Y., Pistidda, C., Gizera, G., Klassen, T. & Dornheim, M. Mg-based materials for hydrogen storage. *J Magnes Alloy* **9**, 1837-1860(2021).

80   Lee, S. Crystal growth of MgB2. *Physica C* **385**, 31-41(2003).

Click here to access/download
Supplementary Material
supporting information.docx

Declaration of interests

☒ The authors declare that they have no known competing financial interests or personal relationships that could have appeared to influence the work reported in this paper.

☐ The authors declare the following financial interests/personal relationships which may be considered as potential competing interests: